Nature Communications

https://doi.org/10.1038/s41467-026-70531-y

Article in Press

Unravelling the Ru-promoted dynamic evolution of Cobalt hydroxide during nitrate reduction towards ammonia production

Received: 20 June 2025

Accepted: 2 March 2026

Cite this article as: Liu, D., Bai, H., Chen, M. *et al.* Unravelling the Ru-promoted dynamic evolution of Cobalt hydroxide during nitrate reduction towards ammonia production. *Nat Commun* (2026). https://doi.org/10.1038/s41467-026-70531-y

Di Liu, Haoyun Bai, Mingpeng Chen, Shuyang Peng, Jiaqian Kang, Lun Li, Ziwen Feng, Chunfa Liu, Weng Fai Ip & Hui Pan

Unravelling the Ru-promoted dynamic evolution of Cobalt hydroxide during nitrate reduction towards ammonia production

Di Liu [1§], Haoyun Bai [2§], Mingpeng Chen [3§], Shuyang Peng [1], Jiaqian Kang [1], Lun Li [1], Ziwen Feng [1], Chunfa Liu [1], Weng Fai Ip [4], and Hui Pan [1, 4*]

[1] Institute of Applied Physics and Materials Engineering, University of Macau, Macao SAR, 999078, China

[2] Center for Materials Science, Queensland University of Technology, Brisbane, QLD, Australia

[3] School of Materials and Energy, Yunnan University, Kunming, 650599, China

[4] Department of Physics and Chemistry, Faculty of Science and Technology, University of Macau, Macao SAR, 999078, China

[§]These authors contributed equally to this work.

*Correspondence

Hui Pan, Institute of Applied Physics and Materials Engineering, University of Macau, Macao SAR, 999078, China

Email: huipan@um.edu.mo

Abstract

Geen ammonia synthesis through electrochemical nitrate reduction (e-NO_3R) using cost-effective Co-based catalysts is promising, but the inevitable structural evolution induced by reductive potentials compromises long-term stability and hinders practical implementation. Focusing on β-$Co(OH)_2$, which serves as the active phase in e-NO_3R systems, this work combines experimental analysis and computational studies to reveal a dynamic surface *OH evolution process: *OH cleavage under negative potentials and *OH generation by the dissociation of NO_3^-. Notably, Ru nanoparticles anchored on β-$Co(OH)_2$ nanosheets promote structural evolution by facilitating *OH cleavage and generation, thereby sustaining a highly active and selective OH-terminated surface. Simultaneously, Ru provides moderate *H adsorption, accelerates the conversions from NO_3^- to NO_2^- and from NO_2^- to NH_3, and thus enhances ammonia synthesis. The optimized $Co(OH)_2$-Ru catalyst achieves an ammonia yield of 98 ± 0.91 $mg \cdot h^{-1} \cdot cm^{-2}$ with a Faradaic efficiency (FE) of 97.7 ± 0.90 % at -0.7 V versus reversible hydrogen electrode (vs. RHE), while maintaining NH_3 FEs above 95% across a broad potential window. This work elucidates structural evolution dynamics, offering a design principle for robust electrocatalysts.

Introduction

Electrochemical nitrate reduction reaction (e-NO_3R) has emerged as a promising strategy for sustainable wastewater remediation and green ammonia (NH_3) synthesis, due to fast reaction kinetics at the solid-liquid interface and weak N=O bond[1,2]. The widespread presence of nitrate contaminants in industrial effluents[3], coupled with recent advances in environmentally friendly nitrate production and concentration technologies[4,5], further enhances the practical viability of this ammonia production pathway. To achieve efficient ammonia production, considerable attention has been devoted to developing efficient e-NO_3R catalysts, including noble metals[6], transition-metal-based materials[7,8], and atomic-level catalysts[9]. Particularly, cobalt(Co)-based catalysts have gained considerable attention in e-NO_3R applications because of their earth abundance, cost-effectiveness, and high ammonia selectivity[10]. However, it has been found that Co-based materials usually undergo severe reconstruction during the e-NO_3R process[11], ultimately compromising long-term catalytic stability and hindering practical implementation in industrial-scale reactors[1,12].

Usually, most Co-based materials reconstruct to β-$Co(OH)_2$ intermediates, pivotal role in catalytic processes[11,13,14]. Intriguingly, advanced characterizations have uncovered dynamic structural cycling between β-$Co(OH)_2$ and metallic Co phases during spontaneous nitrate reduction[15,16], potentially explaining the high catalytic performance of cobalt-based systems. However, atom-level insights into the structural evolution are missing. Therefore, strategies focused on investigating and promoting the evolution of β-$Co(OH)_2$ toward active and stable states offer a more effective approach to enhancing the e-NO_3R performance than precursor modification.

Herein, we developed a series of noble metal-decorated cobalt hydroxide hybrids ($Co(OH)_2$-M). Through in-situ characterizations coupled with density-functional-theory (DFT) simulations, we identified ruthenium (Ru) nanoparticles (NPs) as a promoter during the structural evolution of $Co(OH)_2$ on the surface, which entails concurrent surface *OH cleavage under reduction potential and *OH regeneration through the dissociation pathway of nitrate (NO_3^-). Moreover, Ru NPs in $Co(OH)_2$-Ru systems are found to serve as efficient *H donors, synergistically enhancing both nitrate-to-nitrite and nitrite-to-ammonia conversion kinetics. The optimized $Co(OH)_2$-Ru catalyst achieves performance metrics: >95% Faraday efficiency (FE) for NH_3 production across a broad potential window (-0.1 to -0.7 V vs. reversible hydrogen

electrode (RHE)) and an ammonia yield rate of 98 ± 0.91 $mg \cdot h^{-1} \cdot cm^{-2}$ at -0.7 V[17-22]. This work elucidates the pivotal dual role of Ru in promoting the structural evolution of $Co(OH)_2$ and supplying moderate *H. By correlating structural dynamics with catalytic activity, we establish a mechanistic framework that deepens the understanding of reconstruction-reaction interplay in transition metal electrocatalysts, offering strategic guidance for rational catalyst design.

Results

Electrochemical characterizations

The $Co(OH)_2$-based hybrid catalysts were synthesized through a sequential electrochemical deposition protocol (Figure 1a). Initially, α-$Co(OH)_2$ nanosheets were galvanostatically deposited on nickel foam (NF), forming a hierarchical micro-nano architecture (Figures S1-S2). Subsequent linear sweep voltammetry (LSV) enabled precise loading of noble metal (Ru, Pd, Au) nanoparticles (NPs) onto the α-$Co(OH)_2$ matrix (Figures S3-S4). Meanwhile, our quasi in-situ X-ray diffraction (XRD) patterns indicate that the Ru deposition triggers phase transformation to β-$Co(OH)_2$[23] (Figure S5). The resultant catalysts, designated as $Co(OH)_2$-Ru, $Co(OH)_2$-Pd, and $Co(OH)_2$-Au, respectively, were systematically compared with pristine $Co(OH)_2$. We systematically studied the catalysts for the hydrogen evolution reaction (HER) and e-NO_3R under ambient conditions (room temperature: 25 ± 2 °C) in 1M KOH with and without 0.1 M KNO_3 (Details in Experimental Section, Supporting Information). All measurements were performed without iR compensation. For the HER test, $Co(OH)_2$-Ru requires the least overpotential to reach a given current density (Figure 1b). The LSV curves indicate that all the measured electrodes show higher current density in 1M KOH + 0.1 M KNO_3 than in 1M KOH only, implying the commencement of the e-NO_3R process. For e-NO_3R, Ru decoration greatly reduces the overpotential at 10 $mA \cdot cm^{-2}$, demonstrating that Ru NPs can facilitate the nitrate reduction process. Among these Co-based catalysts, $Co(OH)_2$-Ru outperforms other catalysts in e-NO_3R, realizing a high current density of more than 1.1 $A \cdot cm^{-2}$ at -0.7 V versus (vs.) RHE. Chronoamperometric tests were conducted on $Co(OH)_2$-Ru within the potential range of 0 to -0.7 V vs. RHE to investigate ammonia production and selectivity. Impressively, $Co(OH)_2$-Ru exhibits an ammonia selectivity of more than 95% over a broad potential range of -0.1 to -0.7 V vs. RHE,

surpassing other Co-based catalysts (Figures 1c-1e, S6, & S7). Moreover, $Co(OH)_2$-Ru shows both much higher ammonia selectivity and current density than $Fe(OH)_2$-Ru, $Ni(OH)_2$-Ru, and pure Ru (Ru@NF), further demonstrating that $Co(OH)_2$ plays a key role in improving the NO_3^--to-NH_3 conversion (Figures S8-S9). Importantly, $Co(OH)_2$-Ru achieves a FE of 97.7 ± 0.90 % and a production rate of 98 ± 0.91 $mg \cdot h^{-1} \cdot cm^{-2}$ for NH_3 at -0.7 V vs. RHE (Figure 1c) (Figure 1i, Table S9). Impressively, $Co(OH)_2$-Ru shows high stability under -0.7 V vs. RHE in a cycled stability test for over 100 h (Figures 1f, S10, & S11), where the high ammonia FE (> 90%) and corresponding average ammonia yield (~ 90 $mg \cdot h^{-1} \cdot cm^{-2}$) are sustained (Figure 1g). Furthermore, a home-made nitrate reduction flow cell ($Co(OH)_2$-Ru as cathode for e-NO_3R and NiFe-based layer double hydroxides as anode for oxygen evolution reaction) was assembled to assess the large-scale utilization of $Co(OH)_2$-Ru by only refreshing anolyte[24] (Figures 1g-1h & S12). The flow cell maintains stable operation for over 330 h at 500 $mA \cdot cm^{-2}$ with an NH_3 FE of ~90%. In addition, more than 30% of the produced NH_3 stripped by the natural air stream can be collected in the 1M HCl solution (Figure 1h).

To ensure the ammonia originates from nitrate reduction only, isotopic labeling experiments were conducted and examined by proton nuclear magnetic resonance (^{1}H-NMR) under -0.4 V with $^{14}NO_3^-$ and $^{15}NO_3^-$. The ^{1}H-NMR spectra reveal the distinct peaks for $^{15}NH_4^+$ at δ = 6.80 and 7.04 ppm when the nitrogen source is $^{15}NO_3^-$. Conversely, when $^{14}NO_3^-$ is used as the reactant, the resulting $^{14}NH_4^+$ exhibits a triple peak pattern at δ = 6.83, 6.96, and 7.09 ppm, assigned to $^{14}NH_4^+$ (Figure S16). To investigate the effect of Ru amount in the prepared catalyst on the e-NO_3R activity, the Ru NPs with various loadings were deposited on $Co(OH)_2$ nanosheets via controlling the deposition cycles (10, 30, and 50 cycles), which are denoted as $Co(OH)_2$-Ru10, $Co(OH)_2$-Ru30 and $Co(OH)_2$-Ru50, respectively (Table S1). From the LSV curves, we see that $Co(OH)_2$-Ru30 exhibits higher current density than other catalysts under high applied potential (Figure S17), indicating the optimal synergy between Ru NPs and $Co(OH)_2$. Besides, the reaction kinetics of $Co(OH)_2$ is improved by the deposited Ru NPs, which is demonstrated by the dramatically decreased Tafel slope (Figures 2a & S18). However, the Ru NPs may not directly act as the active sites in the nitrate reduction process, which is demonstrated by the close double-layer capacity (C_{dl}) value with $Co(OH)_2$ (Figures 2b & S19). The in-situ electrochemical impedance spectroscopy (EIS) was

carried out on the Co-based catalysts to unravel the improved reaction kinetics (Figure 2c). Notably, the R_{ct} (charge transfer resistance) values for both $Co(OH)_2$-Ru and $Co(OH)_2$-Pd remain very low at the +0.2V, whereas those of $Co(OH)_2$ and $Co(OH)_2$-Au decrease at 0V, suggesting that the Ru and Pd NPs can facilitate the conversion of NO_3^- to NO_2^-. Moreover, $Co(OH)_2$-Pd has the lowest R_{ct} values at +0.2 V and +0.1 V, while $Co(OH)_2$-Ru has the lowest R_{ct} values at other potentials, indicating that Ru NPs can also facilitate the conversion of NO_2^- to NH_3. Under negative potentials, the HER process is favored, whose competition may affect the NO_3^--to-NH_3 conversion. The e-NO_3R behavior of $Co(OH)_2$-Ru in 1 M KOH with different NO_3^- concentrations helps understand the catalytic mechanism (Figure 2d). Without NO_3^-, the R_{ct} values for HER remain high until a potential of below -0.2 V is applied, indicating the occurrence of the HER process. With the presence of 0.05 M NO_3^- in the electrolyte, the sudden increase in R_{ct} value at -0.2V indicates the competition between e-NO_3R and HER (Figure 2d). When the NO_3^- concentration reaches 0.1 M, the e-NO_3R dominates the reduction process, as evidenced by the reduced R_{ct} values and the close-to-unity NH_3 FEs. It is found that the H_2 FE increases with the increasing applied potential, indicating the competition from HER. When the applied potential is -0.7V, the H_2 FE is still lower than 1.5%, demonstrating HER is greatly suppressed from 0V to -0.7V (Figure S20). With 0.2 M NO_3^-, R_{ct} is further lowered over the range of 0.1 V to -0.5 V, leading to increased current density. But, the final ammonia yield is comparable to that obtained in 0.1 M KNO_3 because of the lower NH_3 FE (Figure S21).

Structural characterizations

To illustrate the structure of $Co(OH)_2$-Ru and the origin of improvement in the e-NO_3R process by deposited Ru, structural characterizations were carried out on as-prepared $Co(OH)_2$-Ru and $Co(OH)_2$-Ru-AS ($Co(OH)_2$-Ru after the 100 h long-term stability). The scanning electron microscope (SEM) and transmission electron microscope (TEM) images reveal that the fabricated catalysts consist of hexagonal metal hydroxide nanosheets with a size of ~500 nm (Figures 3a, 3b & S1). Additionally, a high-resolution transmission electron microscope (HR-TEM) image of $Co(OH)_2$-Ru illustrates that the deposited Ru NPs with an average diameter of 2.5 nm are mostly distributed on the edge of $Co(OH)_2$ nanosheets (Figure 3c). The lattice spacings of 0.237 and 0.251 nm well corresponds to the (001) and (-101) facets of β-$Co(OH)_2$, respectively, while the lattice fringe spacings of 0.201 and 0.234 nm are attributed to the (101) and (100)

planes of Ru NPs[25], respectively (Figures 3c & 3d). Therefore, the coexistence of Ru NPs and $Co(OH)_2$ nanosheets is visually verified for $Co(OH)_2$-Ru (Figures 3e - 3g). For $Co(OH)_2$-Ru-AS, both $Co(OH)_2$ nanosheets and the anchored Ru NPs are well maintained, indicating the high durability in the reaction (Figures 3h - 3j). Interestingly, we can also find the formation of some thin nanosheets surrounding the Ru NPs, whose lattice spacings of 0.237 and 0.250 nm are in good accordance with the (001) and (-101) facets of β-$Co(OH)_2$ (Figure 3k), respectively. The energy-dispersed X-ray spectroscopy (EDX) mappings confirm that the formed nanosheets are Co-based materials (Figures 3l - 3n).

The high-resolution Co 2*p* X-ray photoelectron spectroscopy (XPS) spectrum of as-prepared $Co(OH)_2$-Ru exhibits six peaks, including the 2*p* 3/2 and 2*p* 1/2 peaks of Co^{2+} and Co^{3+}, as well as their corresponding satellite peaks (Figure 3o). More specifically, Co mainly exists as Co^{2+}, which is consistent with the presence of $Co(OH)_2$ on the surface, as indicated by the aforementioned results. Besides, the four peaks assigned to Ru^0 and Ru^{4+} in the high-resolution Ru 3*d* spectrum are sustained after the long-term stability test, further demonstrating the high stability of $Co(OH)_2$-Ru (Figure 3p). The Co 2*p* peaks of $Co(OH)_2$-Ru were shifted towards higher binding energies than those of $Co(OH)_2$, indicating Co atoms lose electrons (Figure 3o). In contrast, the O 2*p* peaks shifted to lower binding energies, demonstrating that O ions gain electrons (Figure 3q). These findings illustrate the simultaneous formation of thin-layer β-$Co(OH)_2$ during the e-NO_3R process, which has not been reported before.

To evaluate the combination of Ru and $Co(OH)_2$, the X-ray adsorption study (XAS) was carried out directly on the as-prepared $Co(OH)_2$-Ru and $Co(OH)_2$-Ru on NF (Figures 4a-4c). However, the signals are too low for quantitative analysis due to the influence from NF. The Ru K-edge-ray Absorption Near-Edge Structure (XANES) spectra show that the Ru exists as Ru nanoparticles, which is in accordance with our transmission electron microscope (TEM) and XPS results. Meanwhile, the Ru nanoparticles connect with the $Co(OH)_2$ lattice via the Ru-O bond, demonstrating the electron transfer at the interface. Furthermore, the Co K-edge XANES spectrum of $Co(OH)_2$-Ru has a center at 7725.0 eV, indicating the pure $Co(OH)_2$ exists on the surface (Figure S22). Differently, the XANES spectrum of $Co(OH)_2$-Ru-AS shows a shifted center at 7727.2 eV, indicating the further oxidation of Co during the stability test, which might be relevant to the newly formed thin-layer $Co(OH)_2$.

To confirm the observation, Raman spectroscopy was employed to reveal the dynamic evolution process of $Co(OH)_2$. The initial spectroscopic analysis of as-prepared samples reveals prominent vibrational signatures of β-$Co(OH)_2$ at 523 cm^{-1} (A_{2u}) and 600 cm^{-1} (E_g)[26,27], while a weak A_{1g} vibrational mode at 690 cm^{-1} suggests partial surface oxidation to Co_3O_4 species under irradiation (Figure S23). After the stability test, the Raman spectra in the low-wavenumber regime (300-2000 cm^{-1}) have no significant alteration (Figure S24a). Furthermore, potential-dependent in-situ Raman characterization confirms the structural integrity of β-$Co(OH)_2$ as its characteristic vibrational features maintain spectral persistence under operational potentials throughout the electrochemical process (Figure 4e). Notably, the spectral interrogation of the high-frequency vibrational regime (3000-3800 cm^{-1}) reveals a pronounced post-stability emergence of a vibrational band centered at 3574 cm^{-1} (Figure S24b), which should be attributed to the A_{1g} stretching mode of the highly ordered O-H bond, corresponding to the newly formed thin-layer β-$Co(OH)_2$ (Figure 3k & S25). This abnormal peak is also observed for $Co(OH)_2$-Pd, with obviously lower peak intensity (Figures S24b & S26). While for $Co(OH)_2$ and $Co(OH)_2$-Au, the O-H bond cannot be observed, demonstrating that Ru and Pd NPs can facilitate the formation of thin-layer $Co(OH)_2$. In addition, we conducted a time-dependent in-situ Raman experiment for $Co(OH)_2$-Ru under working conditions (-0.3 V) in 1M KOH + 0.1M KNO_3 to elucidate the dynamic process (Figure 4d). Spectral monitoring in the hydroxyl stretching regime (3500-3700 cm^{-1}) shows the emergence of a characteristic vibrational band at 3574 cm^{-1} within the initial 5 minutes and demonstrates progressive signal enhancement correlating with temporal evolution (Figure 4e). After that, comparative in-situ Raman analysis of the same $Co(OH)_2$-Ru system in 1 M KOH electrolyte under equivalent potential (-0.3 V vs. RHE) indicates that the initially prominent O-H stretching vibration keeps decreasing with the operation time, indicating consumption of the OH bond under the reduction potential (Figure 4f). Besides, control experiments in 1M KOH show no detectable vibrational signatures in the high wavenumber region, implying that the O-H bond is generated during the e-NO_3R process (Figure S27). The in-situ potential-dependent Raman tests of $Co(OH)_2$-Ru-AS in 1 M KOH + 0.1 M KNO_3 indicate that the O-H stretching vibration keeps declining with the increase of applied potential (Figure S28). Therefore, we conclude that the dynamic evolution process of the O-H bond happens in the e-NO_3R process, which is generated by

the e-NO_3R process, while converted to water due to the reduction potential. Moreover, we carried out a quasi-in-situ Raman characterization to further confirm the correlation between the e-NO_3R reaction and the O-H bond (Figure S29). Analysis of the time-dependent Raman spectra reveals that the peak intensity of the O-H bond exhibits a continuous upward trend during the initial two hours of the reaction. As the reaction time progresses to three hours, the intensity stabilizes, signifying the establishment of a dynamic equilibrium between the formation and decomposition of the O-H bond (Figure S30a). Moreover, the potential-dependent Raman spectra of $Co(OH)_2$-Ru demonstrate that the peak intensity of the O-H bond is positively correlated with the applied potential (Figure S30b). This correlation strongly suggests that the applied potential influences the balance between the generation and consumption of the *OH intermediate.

To elucidate the structural evolution mechanism, two distinct $Co(OH)_2$-Ru samples were synthesized by changing electrolytes (Figure 4g): 1. $Co(OH)_2$-Ru-DD: Prepared using a deuterated water (D_2O)-based electrolyte for both galvanostatic and LSV depositions; 2. $Co(OH)_2$-Ru-DH: Fabricated with D_2O-based electrolyte for galvanostatic deposition and H_2O-based electrolyte for LSV deposition, respectively. Isotopic Raman spectroscopy was conducted in D_2O-dissolved 1 M KOH + 0.1 M KNO_3 electrolyte for these samples along with $Co(OH)_2$-Ru-AS (Figure 4g). The pristine $Co(OH)_2$-Ru-DD and $Co(OH)_2$-Ru-DH do not have obvious O-D or O-H vibration. During the stability test under -0.5 V vs. RHE, the O-D vibration (~ 2640 cm^{-1}) appears and increases for $Co(OH)_2$-Ru-DD and $Co(OH)_2$-Ru-DH, corresponding to the A_{1g} stretching mode of the highly ordered O-D bond in the reconstructed $Co(OD)_2$ thin layers[28]. Notably, The O-H vibration for $Co(OH)_2$-Ru-DH also appears and sustains during the reaction in the D_2O-based electrolyte, indicating that the OH bond in the reconstructed layer is sourced from the original $Co(OH)_2$. Moreover, For the $Co(OH)_2$-Ru-AS, the O-D vibration emerges within the first hour of testing and stabilizes subsequently, while the O-H peak intensity remains constant at levels significantly exceeding that of O-D signal. This disparity implies that the dynamic process of $Co(OH)_2$ is only associated with surface evolution, not the phase transition. To illustrate the evolution mechanism of surface OH species on β-$Co(OH)_2$, the formation of OH vacancies was studied by DFT calculations. It is found that the formation energy of OH_{top} vacancy is 0.05 eV (Figure S30), which can be easily formed

under the reduction potential in alkaline media, leading to the disappearance of the O-H vibration. In contrast, the formation of OH_{side} vacancies requires a higher overpotential (1.5 eV) (Figure S30). Moreover, the Pourbaix diagram was calculated considering the participation of NO_3^- ions[29,30]. It is found that the Co vacancy is hard to form under reduction potential, indicating that the *OH in the subsurface cannot be reduced. Therefore, the O-H peak during the reaction in D_2O-based electrolyte is preserved. Additionally, instead of forming $*NO_3H$ via a direct mechanism for the reduction of $*NO_3$, the $*NO_3$ on OH-ended and Co-terminated surfaces with adjacent Co sites is more likely to be reduced to $*NO_2$+*OH via a dissociation mechanism ($*NO_3 + H^+ + e^- \Rightarrow *NO_2 + *OH$), which shall generate the *OH (Figure S31-S33). From the above discussion, we believe that the *OH is consumed under the negative potential, while generated by the reduction of $*NO_3$ to $*NO_2$+*OH (Figure 4h). Therefore, in pristine $Co(OH)_2$, the hard consumption of $*OH_{side}$ and facile *H adsorption may impede the structural evolution and block active sites for e-NO_3R. In contrast, Ru and Pd NPs facilitate the reduction and regeneration of *OH, maintaining the OH_{side}-ended or Co-ended $Co(OH)_2$ surfaces and promoting the e-NO_3R performance.

Reaction mechanism

Except the effects of Ru NPs in structural evolution, Ru NPs are usually reported to be capable of producing highly active *H under reduction potentials[31,32], which may also promotes the hydrogenation of nitrogenous intermediates towards ammonia synthesis. The existence of *H is firstly probed using electrochemical characterizations. In 1 M KOH, the cyclic voltammetry (CV) curves exhibit a broad oxidation peak corresponding to the oxidation of *H, which includes the absorbed ($*H_{abs}$) and adsorbed hydrogen ($*H_{ads}$)[33] (Figure 5a). Notably, while $Co(OH)_2$-Au and pristine $Co(OH)_2$ exhibit negligible peak areas for *H oxidation, $Co(OH)_2$-Ru shows the observable peak areas for *H oxidation, and $Co(OH)_2$-Pd demonstrates the largest integrated peak area. This significant enhancement suggests that the incorporation of Pd and Ru NPs effectively promotes both the production and storage of *H species, enabling efficient NO_3^--to-NO_2^- conversion via the dissociation mechanism ($*NO_3 + *H \Rightarrow *NO_2 + *OH$), which concurrently generates the *OH and promotes structural evolution during e-NO_3R. Correspondingly, when 0.1 M NO_3^- is introduced in the electrolyte, the oxidation peak disappears in the CV curves of $Co(OH)_2$-Ru and $Co(OH)_2$-Pd, suggesting the efficient utilization of *H in nitrate reduction (Figure 5b). Besides, there is an obvious reduction peak in the CV curve of $Co(OH)_2$-Pd, which should be attributed to the reduction of $*H_{abs}$ in $Co(OH)_2$-Pd[34]. In contrast, there is only $*H_{ads}$ that exists in $Co(OH)_2$-Ru, underscoring its efficient *H utilization for driving structural evolution and ammonia

formation during e-NO_3R. To probe the formation and consumption of *H radicals, in-situ electron spin resonance (ESR) was performed in 1 M KOH with and without 0.1 M NO_3^- at -0.5 V vs. RHE (Figure 5d), using 5-dimethyl-1-pyrroline-N-oxide (DMPO) as the radical trapping reagent. For $Co(OH)_2$-Ru in the absence of NO_3^-, the intensity of the DMPO-H signal increases progressively with reaction time, exhibiting a prominent peak at 1200 s, which confirms the generation and capture of *H during the reaction. For pristine $Co(OH)_2$, only a very weak DMPO-H signal is detectable at 1200 s, indicating that the loaded Ru NPs significantly enhanced *H formation. When NO_3^- is introduced into the electrolyte, the DMPO-H signal intensity decreases markedly under identical conditions, suggesting that the generated *H is consumed in the reaction process. These ESR results clearly demonstrate the generation, enhancement, and subsequent consumption of *H during the e-NO_3R.

To probe the *H dynamics, the operando EIS Bode plots are applied (Figure 5c). The HER process consists of three primary steps: the Volmer step ($H_2O + M + e^- \rightarrow M\text{-}*H + OH^-$) occurs at low frequency ($<10^{0.5}$ Hz), the Heyrovsky step ($H_2O + M\text{-}*H + e^- \rightarrow M + H_2 + OH^-$) occurs at middle frequency ($10^{0.5}$ Hz-$10^{2.5}$ Hz), and the Tafel step ($M\text{-}*H + M\text{-}*H \rightarrow 2\ M + H_2$) cannot be detected by EIS[35,36]. Electrochemical analysis reveals that the Heyrovsky step emerges as the rate-limiting step in the HER over the $Co(OH)_2$-Ru catalyst as applied potential reaches 0 V vs. RHE, indicating the Volmer-Heyrovsky mechanism[37,38]. Therefore, the adsorbed hydrogen species (*H) under the reductive conditions can be facilely formed, but their subsequent conversion to molecular hydrogen (H_2) remains kinetically hindered. With the introduction of 0.1 M NO_3^-, the phase angles are greatly reduced, indicating sufficient consumption of *H and accelerated e-NO_3R process.

Further insights into how *H affects NO_2^--to-NH_3 conversion are gained through online Differential Electrochemical Mass Spectrometry (DEMS), which tracks reaction intermediates on $Co(OH)_2$-Ru and $Co(OH)_2$ during e-NO_3R. During the periodic change of applied potentials between 0.5 and -0.5 V vs. RHE, the mass-to-charge (m/z) signals corresponding to various intermediates, including 30 (NO), 31 (NHO/NOH), 16 (NH_2/O), and 17 (NH_3/OH) emerge during the continuous eight cycles (Figure 5e). This observation allows us to outline the reaction pathways for e-NO_3R on $Co(OH)_2$-Ru and $Co(OH)_2$ as follows: $NO_2^- \rightarrow NO \rightarrow NHO/NOH \rightarrow NH_3$. The similar intermediates detected on both catalysts confirm that the $Co(OH)_2$ plays as the main active site for e-NO_3R (Figure 5f). Moreover, $Co(OH)_2$-Ru displays

more intense signals for nitrogenous intermediates and a lower H_2 signal, confirming that Ru NPs can suppress competing HER and promote e-NO_3R.

Furthermore, to investigate the utilization of *H in e-NO_3R on $Co(OH)_2$-Ru, a free radical inhibitor, tert-butanol (t-BuOH), is employed as a trap for *H[39]. Obvious decreases in NH_3 yields and FEs across applied potentials highlight the role of *H in both NO_3^--to-NO_2^- and NO_2^--to-NH_3 conversions (Figures 5g & S34). Moreover, at -0.5V, the NH_3 yield and FE of e-NO_3R over $Co(OH)_2$-Ru decreases with the increase of t-BuOH concentration, indicating the high importance of *H in e-NO_3R process (Figure S35). For a better understanding of how the e-NO_3R behavior is affected by loaded metal NPs, the NO_2^--to-NH_3 conversion is studied in the presence of 0.1 M NO_2^- ions. $Co(OH)_2$-Ru outperforms pristine $Co(OH)_2$ in NH_3 yield via electrochemical nitrite reduction (e-NO_2R), while $Co(OH)_2$-Pd underperforms, indicating the Ru NPs can facilitate the NO_2^--to-NH_3 conversion, while Pd NPs limit the conversion (Figure 5h & S36). Additionally, $Co(OH)_2$ and $Co(OH)_2$-Au achieve higher NH_3 current densities in the e-NO_2R process than in the e-NO_3R process, signifying NO_3^--to-NO_2^- conversion as the bottleneck for these catalysts (Figure 5i). In contrast, the inferior low e-NO_2R performance of $Co(OH)_2$-Pd indicates the inefficient NO_2^--to-NH_3 conversion. Obviously, $Co(OH)_2$-Ru exhibits comparable NH_3 current densities in both e-NO_3R and e-NO_2R from -0.1 V to -0.5 V, corresponding to the high NH_3 FEs and NH_3 yields in a wide potential window.

Structural and electrochemical characterizations reveal that $Co(OH)_2$ serves as the main active species for the e-NO_3R process in the $Co(OH)_2$-Ru system. Moreover, experimental evidence demonstrates that the Ru NPs provide abundant *H, accelerating the structural evolution of $Co(OH)_2$ and facilitating both the NO_3^--to-NO_2^- and NO_2^--to-NH_3 conversions. However, the detailed reaction process hasn't been investigated. To elucidate the synergy between Ru NPs and $Co(OH)_2$, the in-situ attenuated total reflectance Fourier-transform infrared spectroscopy (ATR-FTIR) was utilized to illustrate the intermediates during e-NO_3R on the $Co(OH)_2$-Ru and $Co(OH)_2$ (Figures 6a & 6b). As the applied potential decreases, the intensities of the downward bands at 1278, 1440, and 1110 cm^{-1} gradually increase, indicating the production of NO_2^-, *NH, and *NH_2O intermediates, respectively[40-43]. Evidently, the signal corresponding to *NH_2O on $Co(OH)_2$-Ru is stronger than those on $Co(OH)_2$, particularly at lower

overpotentials, denoting that Ru incorporation accelerates the NO_2^--to-NH_3 conversion.

Based on the above analysis, we carried out Density-functional-theory (DFT) calculations on the reaction process on the possible $Co(OH)_2$ terminations. As we mentioned above, the $*NO_2$+*OH intermediates can be easily formed on both Co-ended and OH_{side}-ended $Co(OH)_2$ surfaces via the dissociation mechanism, which can be accelerated by *H. In contrast, the conversion to $*NO_3H$ is hard to form on Co-ended $Co(OH)_2$ surface and cannot compete with the adsorption of H on OH_{side}-ended $Co(OH)_2$ surface, indicating hard NO_3^--to-NO_2^- conversions without participation of *H from Ru and Pd NPs. For NO_2-to-NH_3 conversion, we find that the reaction pathways depend on different terminations. On the OH-ended $Co(OH)_2$ surface, the NO_2 is reduced following the pathway: $*NO_2 \rightarrow *ON+*OH \rightarrow *NO \rightarrow *NHO \rightarrow *NH_2O \rightarrow *NH_2O \rightarrow *NH_2+*OH \rightarrow *OH \rightarrow *+H_2O$, where the $*NO_2$ is reduced via a dissociation mechanism (Figure 6c). The rate-limiting step is "$*ON \rightarrow *NHO$", with a low limiting potential of 0.14 eV. In contrast, the reaction pathway on the Co-ended $Co(OH)_2$ surface is $*NO_2 \rightarrow *NO_2H \rightarrow *NO \rightarrow *NHO \rightarrow *NH_2O \rightarrow *O+NH_3 \rightarrow *OH \rightarrow *+H_2O$. Reducing *NHO to $*NH_2O$ becomes the potential-determining step, with a relatively high limiting potential of 0.60 eV, indicating a lower NO_2-to-NH_3 performance than the OH-ended $Co(OH)_2$ surface. Therefore, the excessive *H provided by loaded Pd NPs may facilitate the hard cleavage of OH_{side}, affecting the NO_2-to-NH_3 conversion and thus decreasing the NH_3 FE (Figure 6d). In contrast, Ru NPs generate moderate *H, sustaining the highly active OH_{side}-ended $Co(OH)_2$ surface and promoting the NH_3 FE.

Discussion

In summary, this work elucidates how Ru nanoparticles serve as a dual-functional promoter to alleviate the performance of $Co(OH)_2$ in e-NO_3R. First, Ru accelerates the dynamic evolution of $Co(OH)_2$, directing it toward an OH-terminated surface that is highly active for ammonia synthesis. Second, Ru

provides optimal *H coverage, which concurrently promotes the NO_3^--to-NO_2^- and NO_2^--to-NH_3 conversions. This directed structural evolution and optimal *H are the cornerstones of the performance of $Co(OH)_2$-Ru, which achieves an ammonia yield of 98 ± 0.91 $mg \cdot h^{-1} \cdot cm^{-2}$ with a Faradaic efficiency of 97.7 ± 0.90 % at -0.7 V vs. RHE, while maintaining >95% NH_3 selectivity over a broad potential window. Our findings establish the strategy of steering evolution pathways as a fundamental paradigm for designing advanced electrocatalysts.

Methods

Chemicals and materials

All the chemicals were used without further purification. Cobalt nitrate hexahydrate ($Co(NO_3)_2 \cdot 6H_2O$, AR), ferric nitrate nonahydrate ($Fe(NO_3)_3 \cdot 9H_2O$, AR), nickel nitrate hexahydrate ($Ni(NO_3)_2 \cdot 6H_2O$, AR), ruthenium (III) chloride hydrate ($RuCl_3 \cdot nH_2O$, 37-42%), Potassium tetrachloropalladate (K_2PdCl_4, 98%), Potassium gold(III) chloride ($KAuCl_4$, 98%), and potassium hydroxide (KOH, 95%) were purchased from Aladdin. The Deuterium oxide (D_2O, 99.9 atom% D) was purchased from Sigma-Aldrich.

Synthesis of $Co(OH)_2$ nanosheets

The metal hydroxides were synthesized by electrodeposition on nickel foam (NF, thickness 1.0 mm) via a galvanostatic step. Before the electrodeposition, NF was cut into 2*2 cm^2 and sonicated in ethanol, 3 M HCl solution, and deionized water for 20 min, 10 min, and 20 min, respectively. The electrodeposition was carried out in the electrolyte consisting of 0.15 M $Co(NO_3)_2$ solution. During the electrodeposition, a carbon rod and an Ag/AgCl electrode (saturated in KCl solution) served as the counter and reference electrodes, respectively. A galvanostatic step was conducted at a reduction current density of -10 mA cm^{-2} for 10 min to deposit $Co(OH)_2$ nanosheets, which requires a potential at around -1.2 V vs Ag/AgCl (Figure S30). The loaded $Co(OH)_2$ content ($L_{Co(OH)2}$, mg cm^{-2}) in $Co(OH)_2$-Ru is estimated to be around 32.4 mg cm^{-2}, according to the ICP results by the following formula.

$$L_{Co(OH)_2} = \frac{C_{Co} * V_1 * V_2 * M_{Co(OH)_2}}{V_{aliquot} * A * M_{Co}} \quad (1)$$

Where C_{Co} is the measured concentration of Co in the 2nd diluted solution, V_1, V_2, and $V_{aliquot}$ are the volumes of concentrated HNO_3 solution for dissolving the samples, dilute HNO_3 for measurement, and the initial dissolved solution that was taken and diluted. A is the surface area of the sample, $M_{Co(OH)2,}$ and M_{Co} are the molar mass of $Co(OH)_2$ and Co.

Loading of metallic nanoparticles

The as-synthesized metal hydroxide nanosheets were cleaned by DI water, and then dried in a vacuum heater (< 0.1 psi). A linear sweep voltammetry (LSV) electrodeposition process was used to synthesize the metallic nanoparticles. The electrodeposition was carried out in a 50 mL electrolyte consisting of 1 M KOH solution and 1 mM (n = 225.43, 11 mg) $RuCl_3 \cdot nH_2O$. During the electrodeposition, a carbon rod and a Hg/HgO electrode (saturated in KOH solution) served as the counter and reference electrodes, respectively. An LSV step was conducted from 0 V to -0.6 V at a scan rate of 10 mV s^{-1}, which was cycled for 10, 30, 50 cycles to realize different loading amounts. The loaded Ru content (L_{Ru}, mg cm^{-2}) in

$Co(OH)_2$-Ru is estimated to be around 0.64 mg cm^{-2}, according to the ICP results by the following formula.

$$L_{Ru} = \frac{C_{Ru} * V_1 * V_2}{V_{aliquot} * A} \quad (2)$$

Where C_{Ru} is the measured concentration of Co in the 2nd diluted solution, V_1, V_2, and $V_{aliquot}$ are the volumes of concentrated HNO_3 solution for dissolving the samples, dilute HNO_3 for measurement, and the initial dissolved solution that was taken and diluted. A is the surface area of the sample.

Preparation of $Co(OH)_2$-Ru-DD and $Co(OH)_2$-Ru-DH

The $Co(OH)_2$-Ru-DD and $Co(OH)_2$-Ru-DH samples were prepared using the same protocols with $Co(OH)_2$-Ru. $Co(OH)_2$-Ru-DD was prepared using a deuterated water (D_2O)-based electrolyte for both galvanostatic and LSV depositions (30 cycles), $Co(OH)_2$-Ru-DH was fabricated with D_2O-based electrolyte for galvanostatic deposition and H_2O-based electrolyte for LSV deposition (30 cycles), respectively.

Preparation of NiFe layered double hydroxide (NiFe-LDH)

For NiFe-LDH[24], 0.350 g $Ni(NO_3)_2 \cdot 6H_2O$, 0.162 g $Fe(NO_3)_3 \cdot 9H_2O$ and 0.32 g urea were dissolved in 30 ml deionized water under vigorous stirring, followed by the immersion of a pre-washed NF (1.5 × 2.0 cm^2) into the solution and reaction in a Teflon-lined autoclave at 120 °C for 12 h. After washing with deionized water and drying in a vacuum oven at 25 °C for 12 h, the NiFe-LDH was obtained.

Materials characterization

The morphology and structure were characterized using scanning electron microscopy (SEM, ZEISS, Gemini) and transmission electron microscopy (TEM, JEM-2100). High-angle annular dark field scanning transmission electron microscopy (HAADF-STEM) images with aberration correction were obtained using a Thermo Fisher Spectra 300 with a probe corrector. X-ray diffraction (XRD) was performed using a Cu Kα source X-ray diffractometer (RIGAKU TTRIII). X-ray photoelectron spectroscopy (XPS) analysis was conducted using an Al Kα radiation K-α+ instrument. The elemental composition was determined by inductively coupled plasma optical emission spectroscopy (ICP-OES) using an Agilent 5110 (1.20 kW). Before ICP tests, the sample with a size of ~ 0.02 cm^2 is soaked and sonicated in 5 ml 5 M HNO3 solution. After that, 100 μL of this solution is taken out and diluted in 10 ml 1 M HNO_3 solution for the ICP test. Vibrational characteristics were examined using a Horiba LabRAM HR Evolution Raman system configured for both ex-situ and in-situ measurements. The in-situ Raman analysis was conducted using a 532 nm excitation laser within a customized electrochemical cell consisting of a Hg/HgO reference electrode and graphite counter electrode. The Raman spectra were sequentially collected with progressively varying the potential or prolonging the operating time. Prior to measurements, instrument calibration was verified using the characteristic silicon phonon mode at 520.7

cm^{-1}. The contents of Co and Ru in the $Co(OH)_2$-Ru catalysts with varying LSV cycles were identified using an inductively coupled plasma optical emission spectrometer (ICP-OES, Optima 8000). X-ray absorption fine structure (XAFS) analysis was performed by Shiyanjia Lab using the beamline at the SPring-8 synchrotron radiation source in Japan. The analysis included X-ray absorption near-edge structure (XANES) and extended X-ray absorption fine structure (EXAFS), with further data processing enhanced by K^2-weighted wavelet transform.

^{1}H-NMR measurements were carried out on a Bruker 300 MHz NMR spectrometer. To unravel the origin of ammonia during nitrate reduction, isotope-labeled experiments were performed using Potassium-^{15}nitrate ($K^{15}NO_3$, 99 atom %, Aladdin) as the nitrogen source. The electrochemical nitrate reduction reaction (e-NO3R) was conducted in an electrolyte containing 1 M potassium hydroxide (KOH) mixed with 0.1 M either $K^{14}NO_3$ or $K^{15}NO_3$. After the electrolysis at -0.5 V vs. RHE, a 2 mL aliquot of the post-reaction electrolyte containing the generated $^{14}NH_4^+$ or $^{15}NH_4^+$ was collected. The collected sample was acidified to ~ pH 2 using 4 M H_2SO_4. The quantification of ammonia in the prepared solution was then performed by ^{1}H NMR spectroscopy, using a solvent containing 90% H2O and 10% DMSO-d6 (by volume), with 1 mg of maleic acid added as an internal standard.

The in-situ Electron spin resonance (ESR) spectra were carried out on a Bruker Magnettech ESR5000 system. Before the experiment, 10 mM 5, 5-dimethyl-1-pyrroline N-oxide (DMPO) was added to the catholyte for in-situ capture the instable hydrogen radical. During the experiment, HER on $Co(OH)_2$-Ru operated for 300, 600 and 1200 seconds at -0.5 V vs. RHE in 1 M KOH. 1 mL of the reacted catholyte is taken out and immediately transferred into a glass tube for measurements. ESR spectra of e-NO_3R on $Co(OH)_2$-Ru and HER on $Co(OH)_2$ for 1200 seconds were also conducted for comparison.

Online differential electrochemical mass spectrometry (DEMS) tests were performed on a LingLu 100 by Shiyanjia Lab. Typically, the catalyst was applied to a regular potential change between 0.5 and -0.5 V vs. RHE in 1 M KOH with 0.1 M KNO_3 with an electrolyte flow rate of 3 mL/min, and the mass-to-charge (m/z) signals were collected for analysis (Figure S44). The L-DP01 porous membrane from LingLu instrument is utilized. The signals of various intermediates were collected along during each operation using a Linglu QAS100 mass spectrometer, continuing for a total of eight cycles. The intermediates were carried to the detector using helium as the carrier gas.

In-situ Raman spectroscopy measurements were performed using a GAOSS UNION cell, with a carbon rod and an Hg/HgO electrode serving as the counter electrode and reference electrode, respectively. The electrolyte was 1 M KOH with 0.1 M KNO_3.

In-situ Attenuated Total Reflection Fourier-transform infrared (ATR-FTIR) spectra were measured by using an electrolysis cell with a three-electrode configuration. The obtained materials were used as the working electrode directly, with a Pt wire as the counter electrode and a saturated Ag/AgCl as the reference electrode using a LingLu EC-IR-III cell in a solution of 1 M KOH containing 0.1 M KNO_3. The cell was integrated into a Shimadzu Xross FTIR spectrometer equipped with a liquid nitrogen-cooled MCT detector and attenuated total reflection device (Linglu Co. Ltd., Shanghai, China) using single crystal silicon as ATR crystal. The spectrum obtained at open circuit potential (OCP) serves as the reference. The

potential settings range from 0.1 V to -0.5 V vs. RHE, with intervals of -0.1 V.

Electrochemical characterization

The electrochemical performance of the synthesized catalysts for nitrate reduction reaction was characterized by the electrochemical workstation (ModuLab XM) under ambient conditions (room temperature: 25 ± 2 °C) using an H-type electrochemical cell, which consists of a working electrode, reference electrode on one side, a counter electrode on the other side, and a Celgard 3501 membrane (25 μm, pore size: ~64 nm) as a separator. Before the electrochemical tests, the membrane is cleaned by DI water. During the tests, the fabricated catalysts with a geometric area of 0.25 cm^2 were used as working electrodes, while a platinum foil and a Hg/HgO electrode were utilized as the counter and reference electrodes, respectively. For the e-NO_3R test, each compartment of the H-cell was filled with 40 mL electrolyte (1 M KOH + 0.1 M KNO_3). LSV was conducted from -0.5 V to -2 V versus Hg/HgO at a scan rate of 10 mV s^{-1}, without iR correction, the data is collected every 0.5 seconds without any treatment. Chronoamperometry (i-t) was performed under ambient conditions (room temperature: 25 ± 2 °C) at various potentials for 1 hour to determine the Faradaic efficiency (FE) and ammonia yield rate, the data was collected every 3 seconds without any treatment. The current density was normalized to the geometric area of the working electrode, unless otherwise stated. Recorded electrode potentials versus Hg/HgO were converted to the reversible hydrogen electrode (RHE) scale using the formula: $E_{RHE} = E_{Hg/HgO} + 0.098 + 0.059 \times pH$. When pH =14, the difference is 0.924 V. According to three individual measurements using a calibrated pH meter, the pH of the electrolyte is 13.88 ± 0.01, close to 14. Before each test, the reference electrode is calibrated using fresh Hg/HgO as the counter electrode. The difference is confirmed to be lower than 10 mV. Electrochemical impedance spectroscopy (EIS) measurements were performed in the frequency range of 10 kHz to 0.01 Hz with an amplitude of 10 mV. The electrochemically active surface area (ECSA) was estimated by measuring the double-layer capacitance (C_{dl}) from cyclic voltammetry (CV) at scan rates ranging from 20 to 100 mV s^{-1}. The C_{dl} was calculated by plotting half the difference in current density ($\Delta j/2$) against the scan rates.

The home-made flow cell was assembled with an anode (1.0 cm^2), a cathode (1.0 cm^2), and a Celgard 3501 membrane. $Co(OH)_2$-Ru and NiFe-LDH served as the cathode and anode, respectively. The catholyte containing 1 M KOH + 0.5 M KNO_3 at 25 ± 2 °C was continuously pumped from a 2 L container into the cathode chamber to supply sufficient nitrate ions without refreshing catholyte at a flow rate of 100 $mL \cdot min^{-1}$ via a Kamoer DIpump 550. The overflow from the cathode chamber returned to the container due to the height difference (Figure S30), accompanied by the natural air stream. Both the cathode and anode chambers have a volume of 100 mL. The outlet gas stream was purged into 500 ml of 0.1 M HCl to collect the NH_3 product and a 200 ml pure water to adsorb the residual HCl. The durability test was carried out under ambient conditions (room temperature: 25 ± 2 °C) using an electrochemical workstation (CHI 660e) at a current density of 500 mA cm^{-2} for 339 h. The applied voltage was monitored throughout the durability test through automated acquisition at 3-hour intervals (Figure S31). The amount of NH_3 in all the solutions was measured, and the corresponding Faradaic efficiencies (FE_{cell} and $FE_{collect}$)

were calculated.

For each electrochemical test, the electrolyte was prepared and stored in a dark, dry place for no longer than one week.

Product analysis

The concentrations of Ammonia (NH_3) were quantified via the indophenol blue method using ultraviolet-visible (UV-Vis) spectroscopy. Typically, 20 μL of the catholyte was added to 2 mL of an alkaline solution containing 1 M NaOH, 5 wt.% salicylic acid and 5 wt.% sodium citrate. The mixture was then sequentially combined with 2 mL of deionized water, 1 mL of 0.05 M NaClO solution, and 200 μL of 1 wt.% sodium nitroferricyanide solution. After color development for 30 minutes, the absorbance was measured from 500 nm to 800 nm. The concentrations of NH_3 were determined by interpolating the absorbance values at 655 nm against a calibration curve constructed using standard NH_4Cl solutions with known concentrations (Figure S13, Supplementary Information).

Nitrite (NO_2^-) concentrations were measured using the Griess colorimetric method. 0.16 g of N-(1-naphthyl) ethylene-diamine dihydrochloride and 3.2 g of sulfonamide were dissolved in 80 mL of DI water, which is further mixed with 16 mL of H_3PO_4 to prepare the Griess reagent. For each measurement, 20 μL of catholyte was mixed with 3 mL of H_2O and 1 mL of freshly prepared Griess reagent. In the reaction, sulfonamide reacts with nitrite under acidic conditions to form a diazonium salt, which subsequently couples with the amine to produce a colored azo dye. The absorbance of the resulting solution is recorded from 450 nm to 650 nm. Quantification was achieved by referencing the measured absorbance at 540 nm to a calibration curve generated from standard KNO_2 solutions with known concentrations (Figure S14, Supplementary Information).

For nitrate (NO_3^-) quantification, a 20 μL aliquot of catholyte was first diluted to a total volume of 5.0 mL with deionized water. To the diluted solution, 100 μL of 1 M HCl solution and 10 μL of 0.8 wt.% sulfamic acid solution were added. The absorbance spectrum of the sample was then recorded between 200 and 300 nm. The NO_3^- concentration was calculated based on the difference in absorbance values measured at 220 nm and 275 nm. A standard calibration curve was constructed using KNO_3 solutions of varying concentrations (Figure S15, Supplementary Information).

Calculation of the FEs and yield

For NO_3^--to-NH_3, the Faraday efficiency was determined as follows:

$$FE = \frac{8 \times F \times C(NH_3) \times V}{M_{NH_3} \times Q} \times 100\% \quad (3)$$

For NO_3^--to-NO_2^-:

$$FE = \frac{2 \times F \times C(NO_2^-) \times V}{M_{NO_2^-} \times Q} \times 100\% \quad (4)$$

For NO_2^--to-NH_3:

$$FE = \frac{6 \times F \times C(NO_2^-) \times V}{M_{NH_3} \times Q} \times 100\% \quad (5)$$

where F is the Faraday constant (96485 C mol^{-1}), C is the measured NH_3 or NO_2^- concentration, V is the volume of electrolyte in the cathode compartment (40 mL), M is the molar mass of NH_3 or NO_2^-, and Q is the total quantity of applied electricity (C).

For HER,

$$FE = \frac{2 \times F \times n(H_2)}{Q} \times 100\% \quad (6)$$

where F is the Faraday constant (96485 C mol^{-1}), n is the molar amounts of generated H_2, and Q is the total quantity of applied electricity (C). The molar amounts of generated H_2 was measured by GC (GC-2014, Shimadzu) with a thermal conductivity detector (TCD).

The yield of NH_3 was calculated from:

$$Y_{NH3} = \frac{C(NH_3) \times V}{t \times A} \quad (7)$$

where C is the measured NH_3 concentration, V is the volume of electrolyte in the cathode compartment (40 mL), t is electrolysis time (h), and A effective area of the electrode (cm^2).

The NH_3 partial current density (j_{NH3}) is calculated by the average current density and NH_3 FE using the following formula:

$$j_{NH_3}(mA\ cm^{-2}) = j\ (mA\ cm^{-2}) * FE_{NH_3} \quad (8)$$

Theoretical calculations

First-principle calculations based on density functional theory were carried out using the Vienna Ab initio Simulation Package (VASP) to simulate both the catalytic process and Raman spectra.[44-46] The Perdew-Burke-Ernzerhof (PBE) functional within the generalized gradient approximation (GGA) was employed to describe the exchange-correlation functional. [47] To properly describe the correlation between Co 3d electrons, the DFT+U calculations were carried out with the effective Hubbard U-J parameter (U_{eff}) set to 3.8 eV. [48,49] Structural optimization of bulk $Co(OH)_2$ was initially performed using a plane-wave basis set

with a cutoff energy of 550 eV and a Γ-centered Monkhorst-Pack k-point mesh of 7×7×5.[50] Convergence thresholds were set to 10^{-6} eV for electronic energy and 0.005 eV/Å for ionic forces.

Catalytic processes were simulated using $(\bar{1}01)$ terminated $Co(OH)_2$ slabs, constructed from 3×3×2 primitive unit cells. A vacuum layer of at least 20 Å was introduced to separate the During the structural optimization, the atoms in the top layer were allowed to relax, while the other atoms were constrained. Brillouin zone integration for the slab calculations was performed using a 3×3×1 Monkhorst-Pack k-point mesh. Van der Waals interactions were included via the DFT-D2 correction method throughout all calculations.

As an indicator for each elemental step of e-NO_3R, the Gibbs free energy change (ΔG) is calculated by the following Equation:

$$\Delta G = \Delta E + \Delta ZPE - T\Delta S \quad (9)$$

where ΔE is the total energy change, ΔZPE is the change in zero-point energy, T is temperature 300 K, and ΔS is the difference in entropy.

The calculated Raman spectra of bulk $Co(OH)_2$ was firstly obtained via *raman-sc* code.[51] A key limitation of the DFT+U approach is the sensitivity of the simulated Raman spectra to the selected U value. Consequently, the calculated values are intended only for relative comparison.

Data availability

All the data supporting the findings of this study are available within the article and its Supplementary Information files. Source data are provided with this paper.

References

1 Chen, F.-Y. *et al.* Electrochemical nitrate reduction to ammonia with cation shuttling in a solid electrolyte reactor. *Nature Catalysis* **7**, 1032-1043, doi:10.1038/s41929-024-01200-w (2024).

2 Yu, Y.-Z., Cheng, Y., Cheng, S. & Wu, Z.-Y. Advanced Ruthenium-Based Electrocatalysts for NO Reduction to Ammonia. *Advanced Materials* **37**, 2412363, doi:https://doi.org/10.1002/adma.202412363 (2025).

3 MacFarlane, D. R. *et al.* A Roadmap to the Ammonia Economy. *Joule* **4**, 1186-1205, doi:10.1016/j.joule.2020.04.004 (2020).

4 Xia, R. *et al.* Electrochemical oxidation of nitric oxide to concentrated nitric acid with carbon-based catalysts at near-ambient conditions. *Nature Catalysis*, doi:10.1038/s41929-025-01315-8 (2025).

5 Liu, D. *et al.* Recent Advances in Electrocatalysts for Efficient Nitrate Reduction to Ammonia. *Advanced Functional Materials* **33**, 2303480, doi:https://doi.org/10.1002/adfm.202303480 (2023).

6 Li, J. *et al.* Efficient Ammonia Electrosynthesis from Nitrate on Strained Ruthenium Nanoclusters. *Journal of the American Chemical Society* **142**, 7036-7046, doi:10.1021/jacs.0c00418 (2020).

7 Chen, F.-Y. *et al.* Efficient conversion of low-concentration nitrate sources into ammonia on a Ru-dispersed Cu nanowire electrocatalyst. *Nature Nanotechnology* **17**, 759-767, doi:10.1038/s41565-022-01121-4 (2022).

8 Wang, Y. *et al.* Enhanced Nitrate-to-Ammonia Activity on Copper–Nickel Alloys via Tuning of Intermediate Adsorption. *Journal of the American Chemical Society* **142**, 5702-5708, doi:10.1021/jacs.9b13347 (2020).

9 Zhang, S. *et al.* Fe/Cu diatomic catalysts for electrochemical nitrate reduction to ammonia. *Nature Communications* **14**, 3634, doi:10.1038/s41467-023-39366-9 (2023).

10 Liu, D. *et al.* Electrocatalytic reduction of nitrate to ammonia on low-cost manganese-incorporated Co3O4 nanotubes. *Applied Catalysis B: Environmental* **324**, 122293, doi:https://doi.org/10.1016/j.apcatb.2022.122293 (2023).

11 Qiao, L. *et al.* Nickel-facilitated in-situ surface reconstruction on spinel Co3O4 for enhanced electrochemical nitrate reduction to ammonia. *Applied Catalysis B: Environmental* **340**, 123219, doi:https://doi.org/10.1016/j.apcatb.2023.123219 (2024).

12 Feng, J., Wang, X. & Pan, H. In-situ Reconstruction of Catalyst in Electrocatalysis. *Advanced Materials* **36**, 2411688, doi:https://doi.org/10.1002/adma.202411688 (2024).

13 Zhu, A. *et al.* Facet-Dependent Evolution of Active Components on Spinel Co3O4 for Electrochemical Ammonia Synthesis. *ACS Nano* **18**, 22344-22355, doi:10.1021/acsnano.4c06637 (2024).

14 Fan, Z. *et al.* Interfacial Electronic Interactions Promoted Activation for Nitrate Electroreduction to Ammonia over Ag-Modified Co3O4. *Angewandte Chemie International Edition* **63**, e202410356, doi:https://doi.org/10.1002/anie.202410356 (2024).

15 Han, S. *et al.* Ultralow overpotential nitrate reduction to ammonia via a three-step relay mechanism. *Nature Catalysis* **6**, 402-414, doi:10.1038/s41929-023-00951-2 (2023).

16 Qiao, L. *et al.* In Situ Reconstructed Cu/β-Co(OH)2 Tandem Catalyst for Enhanced Nitrate Electroreduction to Ammonia in Ampere-Level. *Advanced Energy Materials* **14**, 2402805, doi:https://doi.org/10.1002/aenm.202402805 (2024).

17 Wu, S. *et al.* Ag-Co3O4-CoOOH-Nanowires Tandem Catalyst for Efficient Electrocatalytic Conversion of Nitrate to Ammonia at Low Overpotential via Triple Reactions. *Advanced Science* **10**, 2303789, doi:https://doi.org/10.1002/advs.202303789 (2023).

18 Niu, Z. *et al.* Bifunctional copper-cobalt spinel electrocatalysts for efficient tandem-like nitrate reduction to ammonia. *Chemical Engineering Journal* **450**, 138343, doi:https://doi.org/10.1016/j.cej.2022.138343 (2022).

19 Gong, Z. *et al.* Modulating Metal-Nitrogen Coupling in Anti-Perovskite Nitride via Cation Doping for Efficient Reduction of Nitrate to Ammonia. *Angewandte Chemie International Edition* **62**, e202308775, doi:https://doi.org/10.1002/anie.202308775 (2023).

20 He, W. *et al.* Splicing the active phases of copper/cobalt-based catalysts achieves high-rate tandem electroreduction of nitrate to ammonia. *Nature Communications* **13**, 1129, doi:10.1038/s41467-022-28728-4 (2022).

21 Zhang, J. *et al.* Single-entity Electrochemistry Unveils Dynamic Transformation during Tandem Catalysis of Cu2O and Co3O4 for Converting NO3− to NH3. *Angewandte Chemie International Edition* **62**, e202214830, doi:https://doi.org/10.1002/anie.202214830 (2023).

22 He, W. *et al.* Enhanced Nitrate-to-Ammonia Efficiency over Linear Assemblies of Copper-Cobalt Nanophases Stabilized by Redox Polymers. *Advanced Materials* **35**, 2303050, doi:https://doi.org/10.1002/adma.202303050 (2023).

23 Zhang, Z. *et al.* Electrochemical deposition as a universal route for fabricating single-atom catalysts. *Nature Communications* **11**, 1215, doi:10.1038/s41467-020-14917-6 (2020).

24 Li, Z. *et al.* Seed-assisted formation of NiFe anode catalysts for anion exchange membrane water electrolysis at industrial-scale current density. *Nature Catalysis* **7**, 944-952, doi:10.1038/s41929-024-01209-1 (2024).

25 Zhao, S. *et al.* Constructing regulable supports via non-stoichiometric engineering to stabilize ruthenium nanoparticles for enhanced pH-universal water splitting. *Nature Communications* **15**, 2728, doi:10.1038/s41467-024-46750-6 (2024).

26 Gao, P. *et al.* Understanding the Synergistic Effects and Structural Evolution of Co(OH)2 and Co3O4 toward Boosting Electrochemical Charge Storage. *Advanced Functional Materials* **32**, 2108644, doi:https://doi.org/10.1002/adfm.202108644 (2022).

27 Sanchis-Gual, R. *et al.* Crystallographic and Geometrical Dependence of Water Oxidation Activity in Co-Based Layered Hydroxides. *ACS Catalysis* **13**, 10351-10363, doi:10.1021/acscatal.3c01432 (2023).

28 Ze, H. *et al.* In Situ Probing the Structure Change and Interaction of Interfacial Water and Hydroxyl Intermediates on Ni(OH)2 Surface over Water Splitting. *Journal of the American Chemical Society* **146**, 12538-12546, doi:10.1021/jacs.4c00948 (2024).

29 Chong, L. *et al.* La- and Mn-doped cobalt spinel oxygen evolution catalyst for proton exchange membrane electrolysis. *Science* **380**, 609-616, doi:10.1126/science.ade1499 (2023).

30 Persson, K. A., Waldwick, B., Lazic, P. & Ceder, G. Prediction of solid-aqueous equilibria: Scheme to combine first-principles calculations of solids with experimental aqueous states. *Physical Review B* **85**, 235438, doi:10.1103/PhysRevB.85.235438 (2012).

31 Chen, J. *et al.* Reversible hydrogen spillover in Ru-WO3-x enhances hydrogen evolution activity in neutral pH water splitting. *Nature Communications* **13**, 5382, doi:10.1038/s41467-022-33007-3 (2022).

32 Li, J., Ma, Y., Ho, J. C. & Qu, Y. Hydrogen Spillover Phenomenon at the Interface of Metal-Supported Electrocatalysts for Hydrogen Evolution. *Accounts of Chemical Research* **57**, 895-904, doi:10.1021/acs.accounts.3c00762 (2024).

33 Liu, R. *et al.* Defect Sites in Ultrathin Pd Nanowires Facilitate the Highly Efficient Electrochemical Hydrodechlorination of Pollutants by H*ads. *Environmental Science & Technology* **52**, 9992-10002, doi:10.1021/acs.est.8b02740 (2018).

34 Badea, G. E. Electrocatalytic reduction of nitrate on copper electrode in alkaline solution. *Electrochimica Acta* **54**, 996-1001, doi:https://doi.org/10.1016/j.electacta.2008.08.003 (2009).

35 Gong, M. *et al.* Nanoscale nickel oxide/nickel heterostructures for active hydrogen evolution electrocatalysis. *Nature communications* **5**, 4695 (2014).

36 Liang, S., Teng, X., Xu, H., Chen, L. & Shi, J. H* Species Regulation by Mn-Co (OH) 2 for Efficient Nitrate Electro-reduction in Neutral Solution. *Angewandte Chemie* **136**, e202400206 (2024).

37 Li, D. *et al.* Engineering Ruthenium Species on Metal–organic Frameworks for Water Electrolysis at Industrial Current Densities. *Advanced Energy Materials* **15**, 2404714, doi:https://doi.org/10.1002/aenm.202404714 (2025).

38 Wen, Q. *et al.* Engineering a Local Free Water Enriched Microenvironment for Surpassing Platinum Hydrogen Evolution Activity. *Angewandte Chemie International Edition* **61**, e202206077, doi:https://doi.org/10.1002/anie.202206077 (2022).

39 Li, Y. *et al.* Enhancement of nitrate-to-ammonia on amorphous CeOx-modified Cu via tuning of active hydrogen supply. *Advanced Energy Materials* **14**, 2303863 (2024).

40 Guo, X. *et al.* Controlled Defective Engineering on CuIr Catalyst Promotes Nitrate Selective Reduction to Ammonia. *ACS Nano* **18**, 24252-24261, doi:10.1021/acsnano.4c05772 (2024).

41 Wang, M. *et al.* Polynuclear Cobalt Cluster-Based Coordination Polymers for Efficient Nitrate-to-Ammonia Electroreduction. *Journal of the American Chemical Society* **146**, 20439-20448, doi:10.1021/jacs.4c06098 (2024).

42 Xu, J. *et al.* Breaking Local Charge Symmetry of Iron Single Atoms for Efficient Electrocatalytic Nitrate Reduction to Ammonia. *Angewandte Chemie International Edition* **62**, e202308044, doi:https://doi.org/10.1002/anie.202308044 (2023).

43 Hao, R. *et al.* Elucidation of the electrocatalytic activity origin of Fe3C species and application in the NOx full conversion to valuable ammonia. *Chemical Engineering Journal* **467**, 143371, doi:https://doi.org/10.1016/j.cej.2023.143371 (2023).

44 Kohn, W. & Sham, L. J. Self-Consistent Equations Including Exchange and Correlation Effects. *Phys. Rev.* **140**, A1133-A1138, doi:10.1103/physrev.140.a1133 (1965).

45 Hohenberg, P. & Kohn, W. Inhomogeneous Electron Gas. *Phys. Rev.* **136**, B864-B871, doi:10.1103/physrev.136.b864 (1964).

46 Kresse, G. & Furthmüller, J. Efficient iterative schemes for ab initiototal-energy calculations using a plane-wave basis set. *Physical Review B* **54**, 11169-11186, doi:10.1103/physrevb.54.11169 (1996).

47 Perdew, J. P., Burke, K. & Ernzerhof, M. Generalized Gradient Approximation Made Simple. *Phys Rev Lett* **77**, 3865-3868, doi:10.1103/physrevlett.77.3865 (1996).

48 Li, F., Ai, H., Liu, D., Lo, K. H. & Pan, H. Enhanced oxygen evolution reaction on 2D CoOOH via strain engineering: an insightful view from spin state transition. *Journal of Materials Chemistry A*,

doi:10.1039/d1ta03412j (2021).

49 Friebel, D. *et al.* Identification of Highly Active Fe Sites in (Ni,Fe)OOH for Electrocatalytic Water Splitting. *Journal of the American Chemical Society* **137**, 1305-1313, doi:10.1021/ja511559d (2015).

50 Monkhorst, H. J. & Pack, J. D. Special points for Brillouin-zone integrations. *Physical Review B* **13**, 5188-5192, doi:10.1103/physrevb.13.5188 (1976).

51 *vasp_raman.py*. (https://github.com/raman-sc/VASP/, 2013).

Acknowledgements

This work was supported by the Science and Technology Development Fund (FDCT) from Macau SAR (0050/2023/RIB2, 0023/2023/AFJ, 0002/2024/TFP, and 0111/2022/A2), and Multi-Year Research Grants (MYRG-GRG2025-00007-IAPME and MYRG-GRG2024-00038-IAPME) from the University of Macau, issued to Dr. H. Pan. Dr. W. F. Ip acknowledges support from the Science and Technology Development Fund (0087/2024/AFJ). The DFT calculations are performed at High-Performance Computing Cluster (HPCC) of Information, Communication Technology Office (ICTO) at University of Macau.

Institute of Applied Physics and Materials Engineering, University of Macau, 999078, Macao SAR, China
Di Liu, Shuyang Peng, Jiaqian Kang, Lun Li, Ziwen Feng, Chunfa Liu & Hui Pan*

Center for Materials Science, Queensland University of Technology, Brisbane, QLD, Australia
Haoyun Bai

School of Materials and Energy, Yunnan University, Kunming, 650599, China
Mingpeng Chen

Department of Physics and Chemistry, Faculty of Science and Technology, University of Macau, Macao SAR, 999078, China
Weng Fai Ip & Hui Pan*

Author Contributions

D.L., H.B. and M.C. contributed equally to this manuscript. D.L. and H.P. conceived the idea. D.L. and M.C. contributed to the experimental design, material synthesis, electrochemical measurements, data analysis, TEM and XAFS characterization, and drafting of the initial manuscript. H.B. and D.L. designed and performed the theoretical calculations and also contributed to writing the initial draft. S.P., J.K., L.L., Z.F., and C.L. assisted with XRD and XPS characterization and contributed to editing the draft. W.I. and H.P. provided overall supervision of the project and revised the manuscript. All authors discussed the results and commented on the manuscript.

Correspondence to Hui Pan.

Competing interest

The authors declare no competing interests.

Figure captions

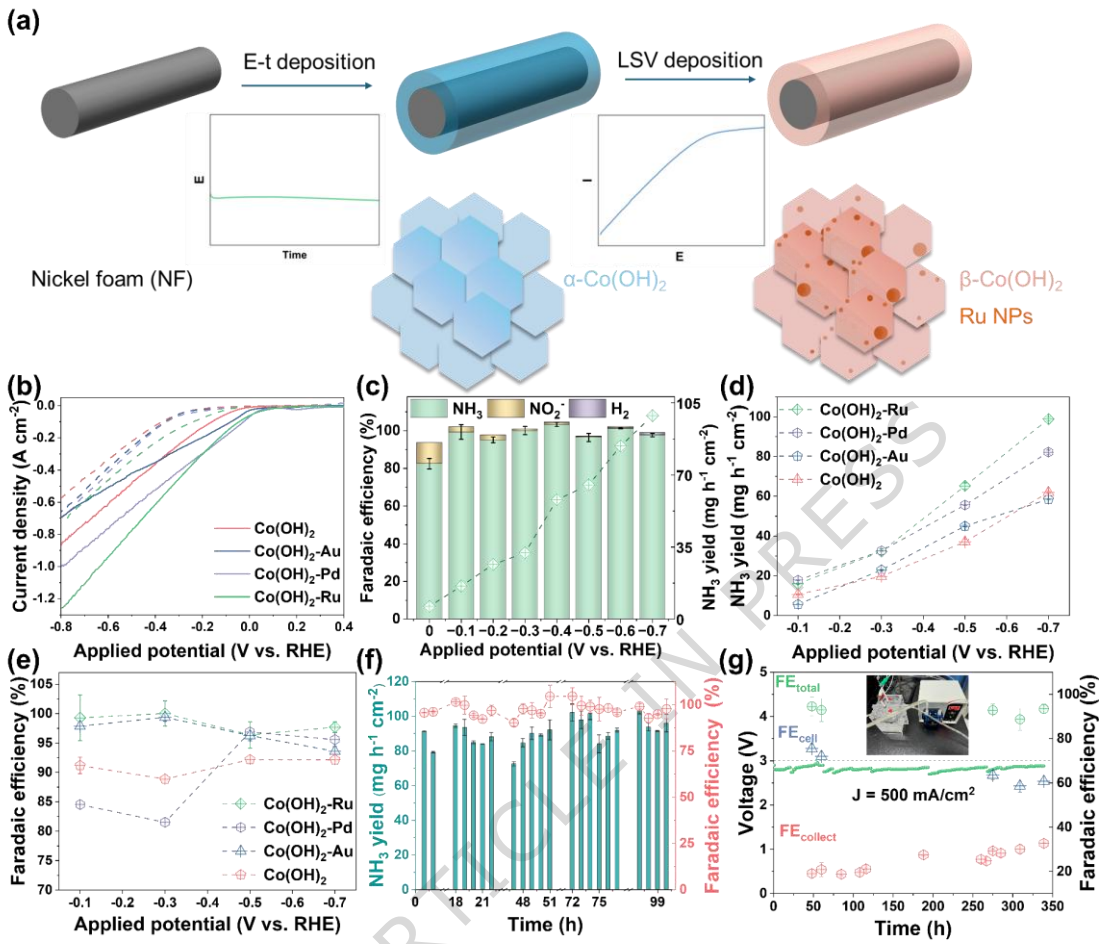

Figure 1. Electrocatalytic performance. a) The schematic illustration for preparing $Co(OH)_2$-Ru via a two-step electrodeposition strategy. b) LSV curves without iR-correction of $Co(OH)_2$-Ru, $Co(OH)_2$-Pd, $Co(OH)_2$-Au, and $Co(OH)_2$ in 1 M KOH with (solid line) and without (dashed line) 0.1 M KNO_3 at a scan rate of 10 mV s^{-1}. c) FEs for NH_3, NO_2^-, H_2, and NH_3 yields of $Co(OH)_2$-Ru at different applied potentials. The error bars of FEs were derived from three individual measurements. d) NH_3 yields and e) NH_3 FEs on $Co(OH)_2$-Ru, $Co(OH)_2$-Pd, $Co(OH)_2$-Au, and $Co(OH)_2$. The error bars of FEs and yields were derived from three individual measurements. f) NH_3 yields and FEs of $Co(OH)_2$-Ru during stability test for 100 h at -0.7 V vs. RHE. The error bars of NH_3 FEs and yields were derived from three individual measurements. g) Applied voltages, NH_3 FEs of $Co(OH)_2$-Ru during stability test in a home-made flow cell for over 330 h at -0.7 V vs. RHE, inset is the photo of the flow cell. The error bars of FEs were derived from three individual measurements. Source data for Fig. 1 are provided as a Source Data file.

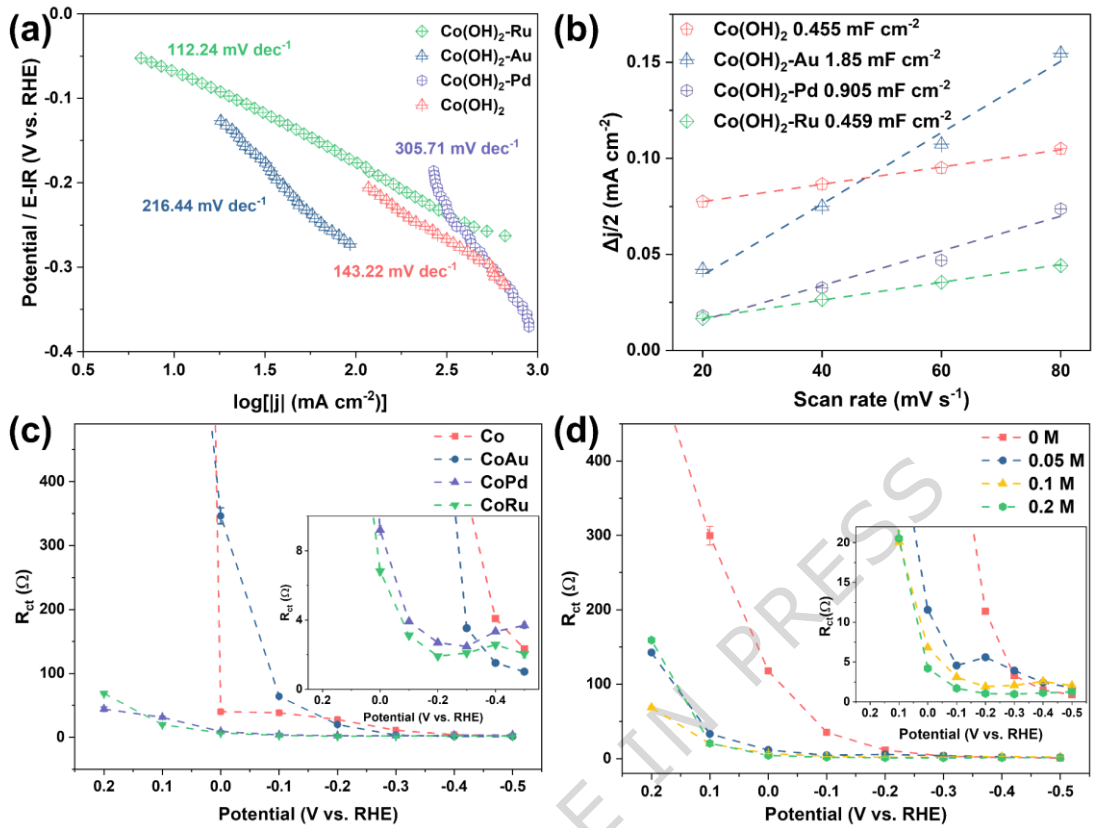

Figure 2. Reaction kinetics. a) Tafel plots with 80% iR correction, b) C_{dl}, and c) the potential-dependent R_{ct} of $Co(OH)_2$-Ru, $Co(OH)_2$-Pd, $Co(OH)_2$-Au, and $Co(OH)_2$ in 1 M KOH with 0.1 M NO_3^-. The error bars for R_{ct} were derived from equivalent-circuit fitting. d) The NO_3^- concentration-dependent R_{ct} values of $Co(OH)_2$-Ru in 1 M KOH with various NO_3^- concentrations. The error bars for R_{ct} were derived from equivalent-circuit fitting. Source data for Fig. 2 are provided as a Source Data file.

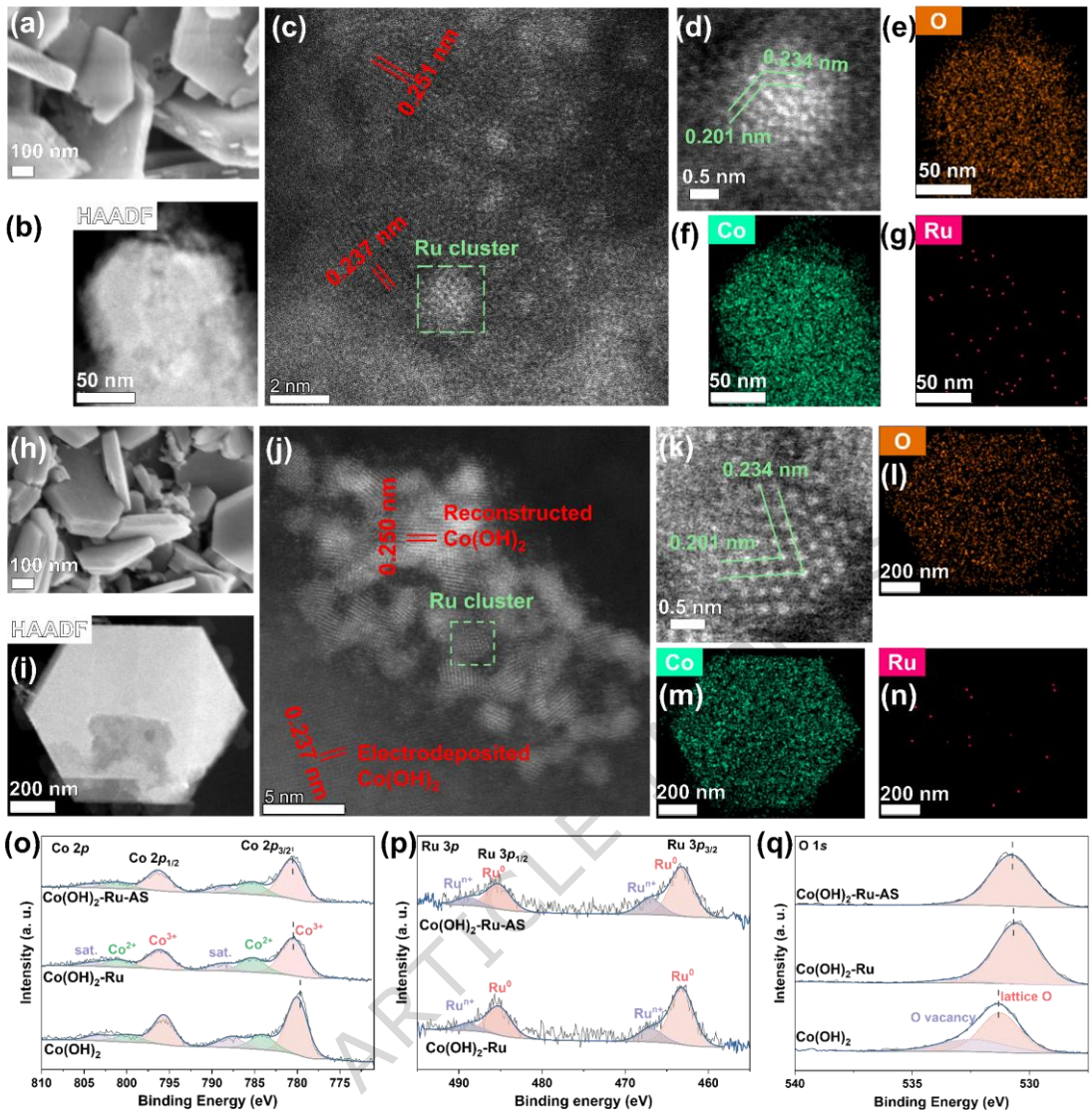

Figure 3. Structural characterizations. Characterizations of as-prepared $Co(OH)_2$-Ru: a) SEM image, b) HAADF-STEM image, c and d) HRTEM images, and e-g) EDX elemental mappings. Characterizations of $Co(OH)_2$-Ru after 100 h stability test: h) SEM image, i) HAADF-STEM image, j and k) HRTEM images, and l-n) EDX elemental mappings. (o) Co 2*p*, (p) Ru 3*p*, and (q) O 1*s* XPS spectra of $Co(OH)_2$, $Co(OH)_2$-Ru and $Co(OH)_2$-Ru-AS. Source data for Fig. 3 are provided as a Source Data file.

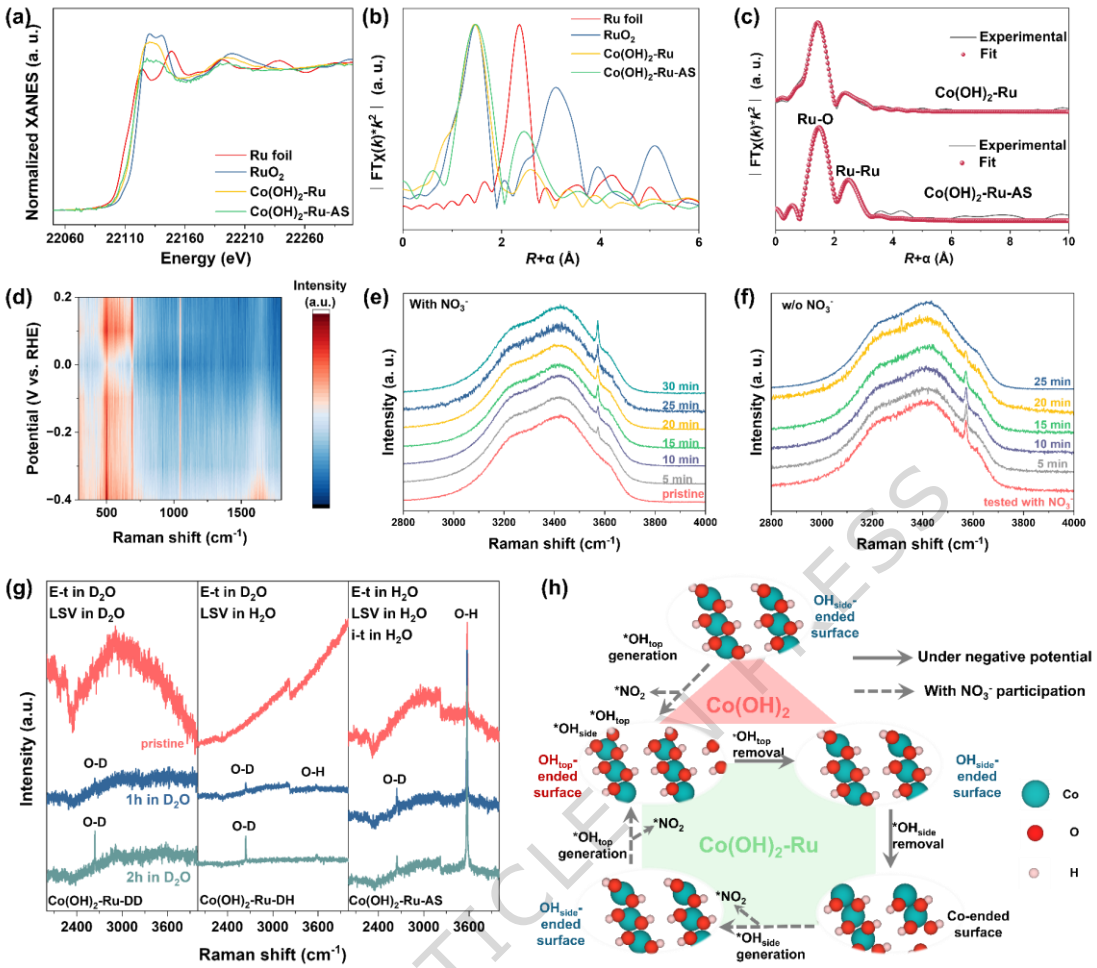

Figure 4. Spectroscopic Characterizations. a) Normalized Ru K-edge XANES of $Co(OH)_2$-Ru, $Co(OH)_2$-Ru-AS, RuO_2, and Ru foil. b) The Normalized k^2-weighted Fourier-transformed Extended X-ray Absorption Fine Structure (FT-EXAFS) spectra of Ru K-edge. c) FT-EXAFS fitting curves in R space of $Co(OH)_2$-Ru, $Co(OH)_2$-Ru-AS. d) Potential-dependent in-situ Raman spectra over $Co(OH)_2$-Ru. Time-dependent in-situ Raman spectra of $Co(OH)_2$-Ru in e) 1M KOH + 0.1 M KNO_3 and f) 1M KOH. g) Time-dependent in-situ Raman spectra for $Co(OH)_2$-Ru-DD, $Co(OH)_2$-Ru-DH, and $Co(OH)_2$-Ru-AS in the electrolyte consisting of 1M KOH, 0.1 M KNO_3, and deuterated water (D_2O). h) The schematic illustration for the dynamic evolution of $Co(OH)_2$ of $Co(OH)_2$ and $Co(OH)_2$-Ru in the e-NO_3R process. Source data for Fig. 4 are provided as a Source Data file.

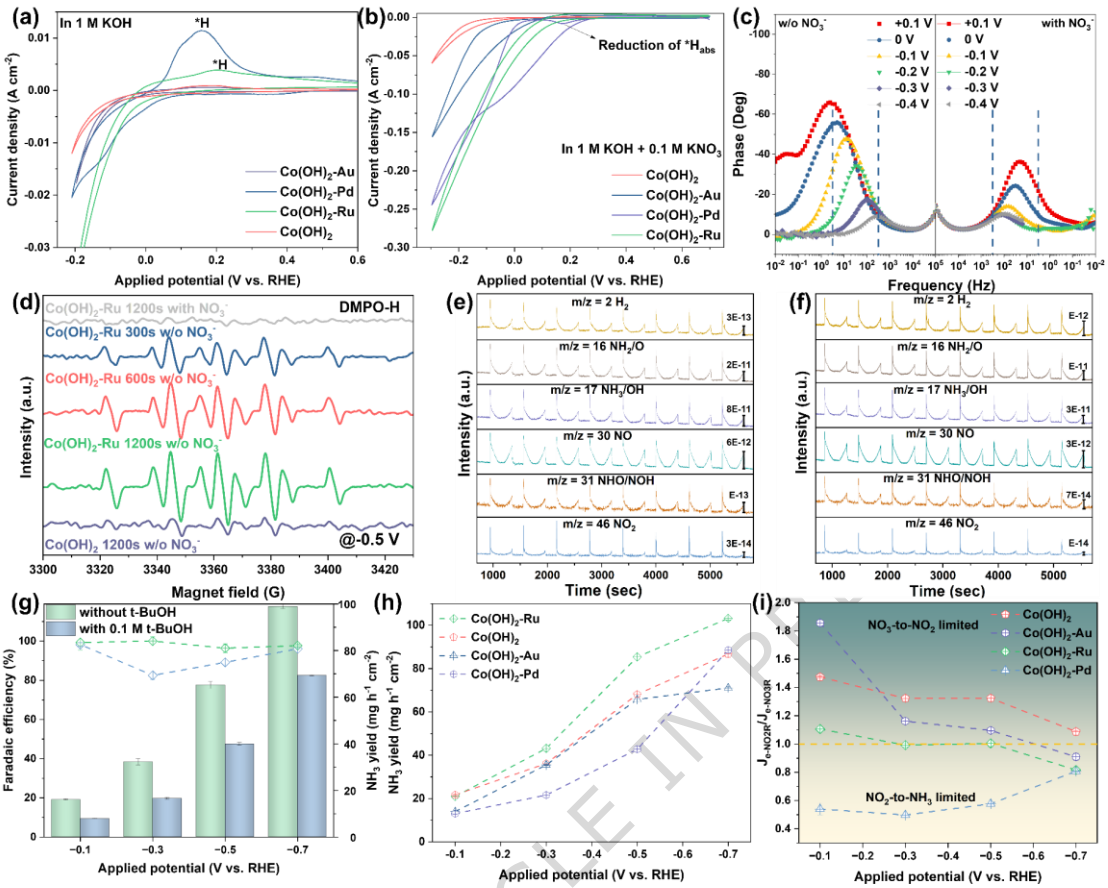

Figure 5. Characterizations of *H production and utilization. a) CV curves without iR-correction of $Co(OH)_2$-Ru, $Co(OH)_2$-Pd, $Co(OH)_2$-Au, and $Co(OH)_2$ in 1 M KOH, scan rate: 5 mV s^{-1}, b) CV curves without iR-correction of $Co(OH)_2$-Ru, $Co(OH)_2$-Pd, $Co(OH)_2$-Au, and $Co(OH)_2$ in 1 M KOH with 0.1 M KNO_3, scan rate: 5 mV s^{-1}. c) Potential-dependent Bode plots of $Co(OH)_2$-Ru in 1 M KOH with and without 0.1 M NO_3^-. d) ESR spectra of the electrolyte catalyzed by $Co(OH)_2$-Ru, and $Co(OH)_2$ in 1 M KOH with/without 0.1 M NO_3^- at -0.5 V vs. RHE. Online DEMS spectra of e) $Co(OH)_2$-Ru, and f) $Co(OH)_2$ in 1 M KOH with 0.1 M KNO_3. g) FEs for NH_3, and NH_3 yields of $Co(OH)_2$-Ru at different applied potentials with and without the addition of 0.1 M t-BuOH. The error bars of FEs were derived from three individual measurements. h) NH_3 yields over $Co(OH)_2$-Ru in 1 M KOH + 0.1 M KNO_2. The error bars of yields were derived from three individual measurements. i) The ratio between NH_3 partial current density of $Co(OH)_2$-Ru in e-NO_2R (J_{NO2R}) and e-NO_3R (J_{NO3R}). The error bars of ratios and yields were derived from three individual measurements and calculations. Source data for Fig. 5 are provided as a Source Data file.

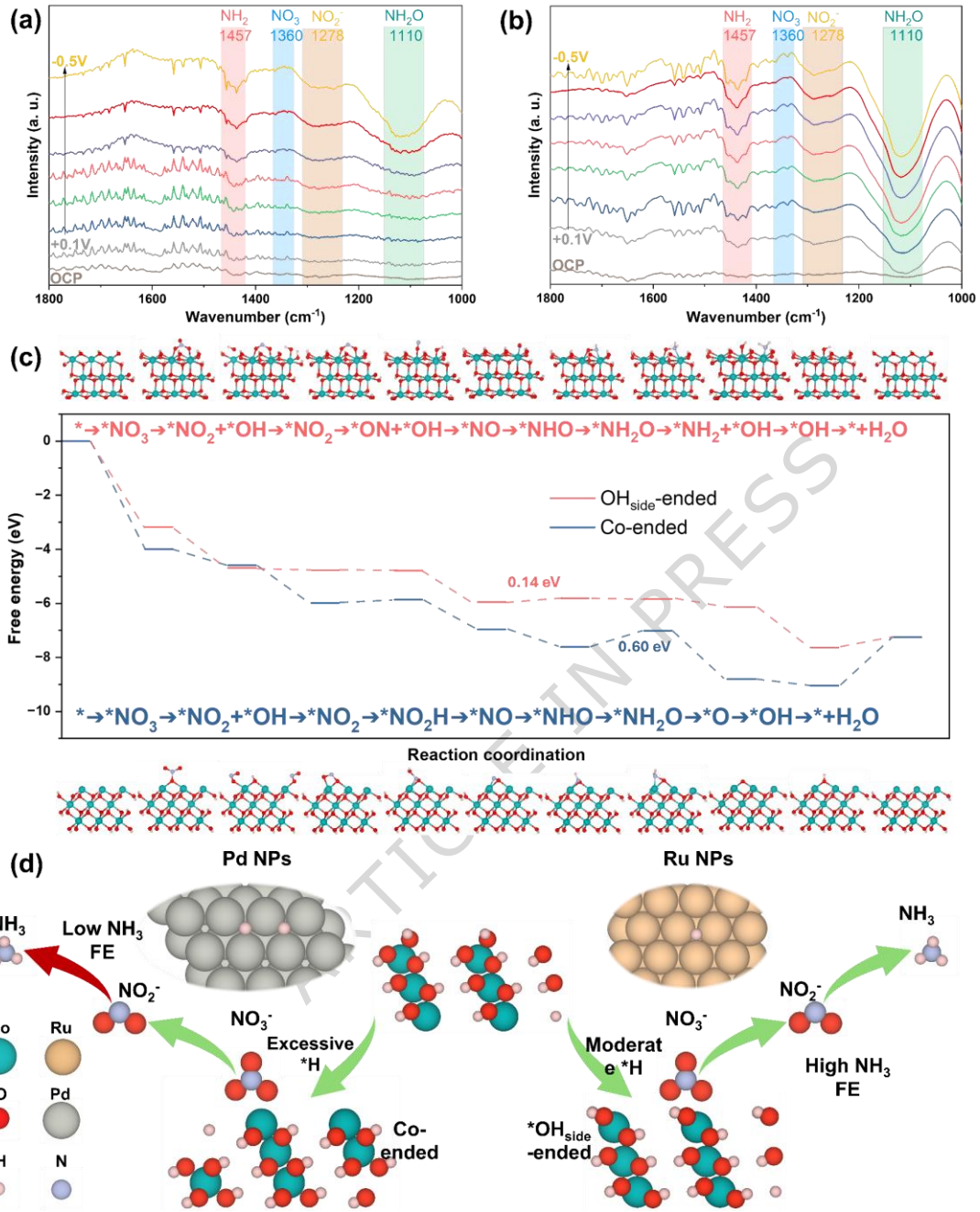

Figure 6. Reaction pathway. The in-situ FTIR spectra of a) $Co(OH)_2$ and b) $Co(OH)_2$-Ru; c) The Gibbs free energy profiles for e-NO_3R on OH_{side}-ended and Co-ended $Co(OH)_2$. (cyan: cobalt; red: oxygen; white: hydrogen; gray: nitrogen). d) The proposed evolution process and reaction mechanism on $Co(OH)_2$-Pd and $Co(OH)_2$-Ru. Source data for Fig. 6 are provided as a Source Data file.

Editor's Summary:

The unclear structural evolution mechanism of Cobalt-based materials restricts the long-term applications of nitrate reduction for ammonia synthesis. Here, the authors report a Ru-promoted dynamic evolution of cobalt hydroxides that can stably produce ammonia at high current densities.

Peer review information: *Nature Communications* thanks Yijun Yang and the other anonymous reviewer(s) for their contribution to the peer review of this work. A peer review file is available.